WILEY | Hindawi

Research Article

The Tight Sand Reservoir Characteristics and Gas Source in Coal Measures: A Case Study of Typical Areas in China

Zengqin Liu [1,2] **Shaobin Guo,**[3] **Yiming Huang,**[4] **Zhe Cao,**[1] **Talihaer· Yeerhazi,**[3] **and Weifu Cao**[5]

[1]*Petroleum Exploration and Production Research Institute, Sinopec, Beijing 102206, China*
[2]*Sinopec Key Laboratory of Shale Oil/Gas Exploration and Production, Beijing 102206, China*
[3]*School of Energy Resources, China University of Geosciences, Beijing 100083, China*
[4]*No.1 Oil Production Plant, Daqing Oilfield Co., Ltd., Daqing 163001, China*
[5]*Exploration and Development Research Institute, PetroChina Daqing Oilfield Company, Daqing 163712, China*

Correspondence should be addressed to Zengqin Liu; zengqin_alex_liu@163.com

Interbedded sandstones, shales, and coal seams were formed in marine-continental transitional environments of coal measures, and the gas source of its tight sand gas has been uncertain, which hinders the progress of natural gas exploration. This article uses the Longtan tight sand gas in west Guizhou as an example to investigate the reservoir features, gas charging history, and main source rock of tight sand gas by examining thin sections, scanning electron microscopy images, X-ray diffraction results, and the fluid inclusions with burial and thermal histories and noble gas analysis. The Longtan sandstones in this study are classified as litharenites which are characterized by low compositional and textural maturities, and high clay contents, and are distinguished petrographically from conventional sandstones by the extensive existence of micropores and microfractures. The results of the homogenization temperatures of the fluid inclusions show that the Longtan tight sand gas is a single-stage accumulation which occurred during the Late Triassic. Furthermore, through the analysis of the helium and argon isotopes of noble gases, a calculation model was established for determining the shale and coal contributions to the tight sand gas. The research results show that the Longtan tight sand gas mainly belongs to the crust-derived gas, mostly from the Longtan shale-derived contribution and to a lesser extent from the Longtan coal-derived contribution. The measured $^{40}Ar/^{36}Ar$ values of the Longtan shales and coals are consistent with the forecasted $^{40}Ar/^{36}Ar$ values from the calculation model, demonstrating that the model is viable to calculate the source rock contribution to the tight sand gas. Therefore, the Longtan shales as main source rocks can generate hydrocarbons to charge neighboring tight sandstones to form tight gas accumulation in the Longtan Formation, which provides an opportunity for tight gas development in west Guizhou.

1. Introduction

Tight sand gas resources in the world are abundant and widely distributed and are an important part of natural gas resources [1, 2]. Tight sand gas accumulations have been widely discovered in a number of basins in the United States and China, such as in the Greater Green River and San Juan Basins in the United States and the Ordos, Sichuan, Tarim, and Songliao Basins in China, all of which have been elaborately studied [3–5]. These tight gas sandstones were mainly deposited in marine or terrestrial environments [5, 6]. However, compared with discoveries in marine and terrestrial tight sandstones, fewer discoveries have been made in marine-continental transitional environments. Marine-continental transitional formations are widely distributed in China, such as the Upper Permian Longtan Formation in South China and the Lower Permian Taiyuan Formation in the Ordos Basin [7]. These formations consist of tight sandstones, shales, and coals and are considered to be potential targets for unconventional resources [7, 8]. However, the
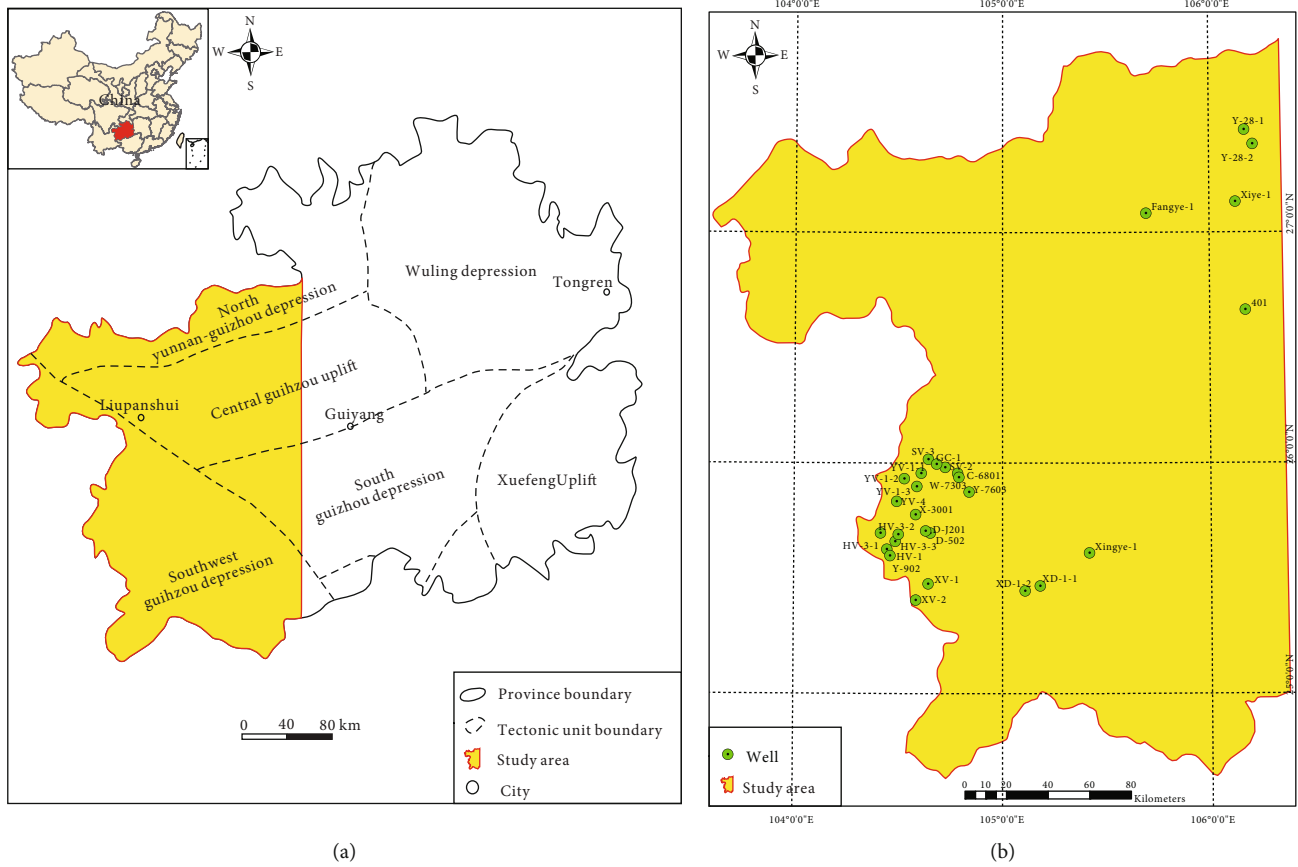
(a)

(b)

Figure 1: Regional sketch map showing (a) major tectonic units (modified from Luo et al. [29]) and our study area in the Guizhou Province and (b) well (green-filled circle) locations in the study area.

gas resources of tight sandstones are poorly understood, which hinders the progress of tight gas development in marine-continental transitional environments.

The resource potential and productivity of tight sandstones can be appraised with a thorough understanding of reservoir characteristics and gas source which contribute to natural gas migration and accumulation [9–11]. A variety of techniques (e.g., X-ray diffraction (XRD) analysis, thin sections, and scanning electron microscopy (SEM)) have been used to characterize the reservoir characteristics to provide an early determination for resource potential of tight sandstones [12, 13]. To establish the relationships between tight sand gas and source rocks, techniques involving fluid inclusions [14–17] and noble gas isotopes [18–21] have been used to evaluate the charging periods and identify the main source rocks of hydrocarbon accumulations. Fluid inclusions have been captured in reservoirs and evolved in a relatively closed system without interference during a certain range of burial, and thus, their composition, temperature, and pressure data can provide important insights into its oil and gas migration and accumulation relative to burial history [17, 22, 23]. Noble gases (e.g., helium and argon) in reservoirs that originate from different sources (e.g., mantle, source rock, and atmosphere) are isotopically distinct and resolvable, owing to different radioelement concentrations (e.g., uranium) in their sources. Furthermore, noble gases preserve a record of their presence and origin because they

do not chemically react with other substances during migration and accumulation history and, therefore, can be used as reliable tracers to correlate source rocks and hydrocarbon accumulations and to resolve different source contributions to noble gases in reservoirs [24–27].

The assemblages of Longtan sandstones, shales, and coals are widely recognized in west Guizhou, China. Previous research results indicate that tight sand gas [28], shale gas [29, 30], and coalbed methane [31] show good potential for unconventional resource development in west Guizhou. A number of wells in west Guizhou have penetrated good gas pays in the Longtan Formation, e.g., the X1 well had gas show values of 20%-30% [8]. However, the ambiguity of tight sand gas potential hinders the development of tight sand gas in west Guizhou. Therefore, the aim of this study is to investigate the reservoir characteristics, charging history, and source rock contribution of tight sand gas in the Longtan Formation in west Guizhou by using various techniques involving thin sections, SEMs, XRDs, fluid inclusions, and noble gas isotopes.

2. Geological Setting

Guizhou Province is located in the Upper Yangtze Platform, South China (Figure 1(a)). Tectonically, it can be subdivided into six major structural units, which, from north to south, are the North Yunnan-Guizhou depression, Wuling
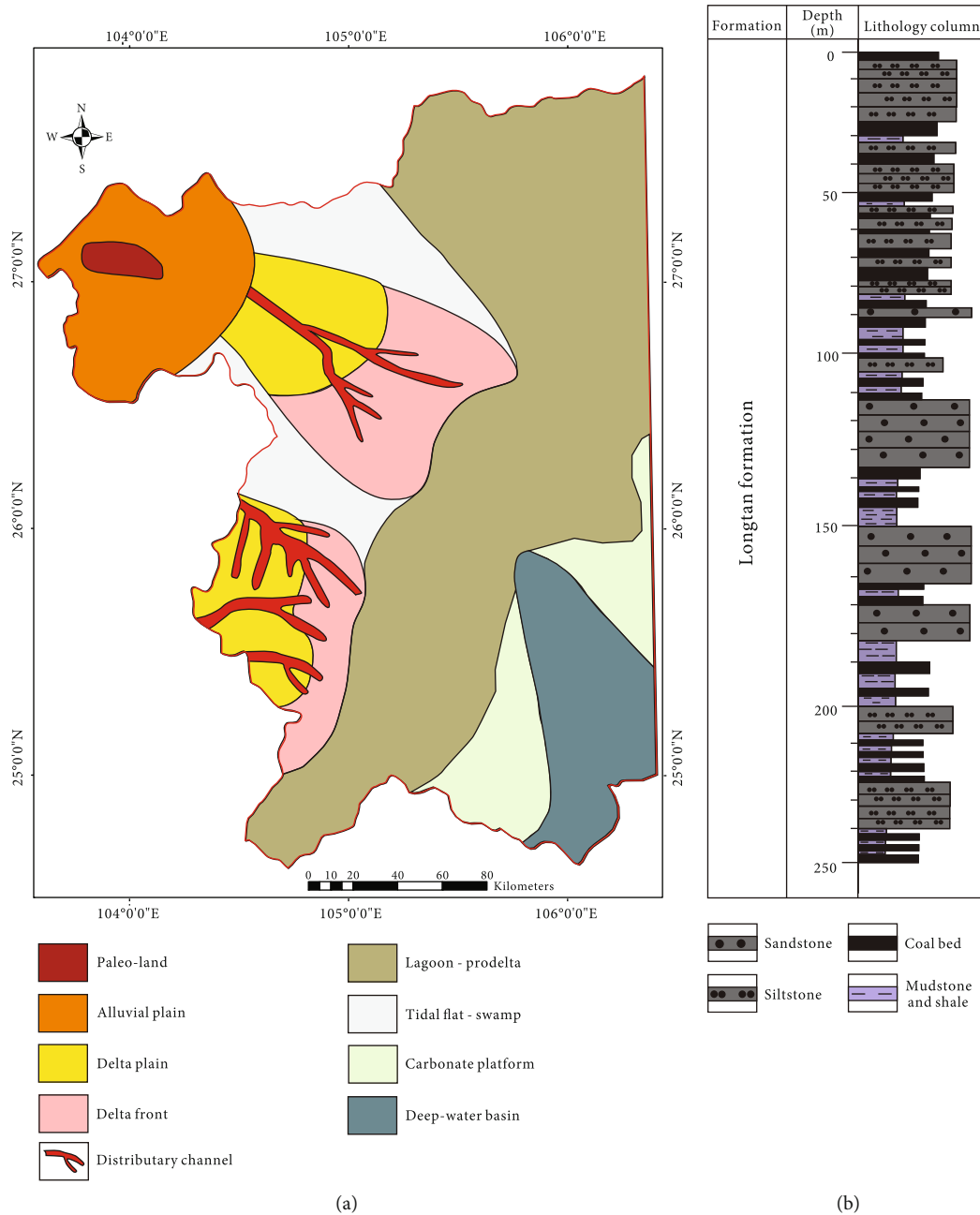
FIGURE 2: The sedimentary environments (modified from Shen et al. [38]) and lithology types of the Longtan Formation in west Guizhou: (a) paleogeography map of the Upper Permian Longtan Formation in the study area and (b) typical lithological column of the Longtan Formation in the study area.

depression, Central Guizhou uplift, Southwest Guizhou depression, South Guizhou depression, and Xuefeng uplift (Figure 1(a); [29, 32]). Our study area, as shown in Figure 1 (yellow area), mainly includes the Southwest Guizhou depression and part of the Central Guizhou uplift, and it consists of 24 wells (Figure 1(b)). From the Sinian to Permian, a thick marine sedimentary section was deposited in this area, followed by long-term weathering and denudation, which were caused by uplift from the Early to Middle Permian [29, 31]. During the Late Permian, a rapid transgression led to the deposition of thick marine-continental sediments in west Guizhou [33]. The Upper Permian Long-

tan Formation experienced multiple stages of tectonic movements, such as the Late Yanshanian ca. 140Ma, the Early Himalayan ca. 80 Ma, and the Late Himalayan ca. 3 Ma [34].

The Upper Permian Longtan Formation was widely deposited in west Guizhou and formed under a variety of settings, including an alluvial plain, a delta, and a tidal flat lagoon (Figure 2(a); [35]). The Longtan Formation consists of interbedded tight sandstones, siltstones, shales, and coal seams (Figure 2(b)), which can form multiple sets of source-reservoir-seal assemblages [7, 36]. Shales and coal seams in the Longtan Formation have good potential for generating gas because they display high total organic

TABLE 1: Summary of the analytical methods employed for the 11 samples.

| Sample	Formation	Lithology	Analytical methods
YV-1-1	Longtan	Sandstone	Porosity & permeability, thin section, SEM, XRD, and fluid inclusion
YV-1-2	Longtan	Sandstone	Porosity & permeability, thin section, SEM, XRD, and fluid inclusion
YV-1-3	Longtan	Sandstone	Porosity & permeability, thin section, SEM, XRD, fluid inclusion, and noble gas isotope
HV-3-1	Longtan	Sandstone	Porosity & permeability, thin section, SEM, XRD, fluid inclusion, and noble gas isotope
HV-3-2	Longtan	Shale	Noble gas isotope
HV-3-3	Longtan	Coal	Noble gas isotope
YV-4	Longtan	Sandstone	Porosity & permeability, thin section, SEM
Y-28-1	Longtan	Sandstone	Porosity & permeability, thin section, SEM
Y-28-2	Longtan	Sandstone	Porosity & permeability, thin section, SEM
XD-1-1	Longtan	Sandstone	Porosity & permeability, thin section, SEM
XD-1-2	Longtan	Sandstone	Porosity & permeability, thin section, SEM
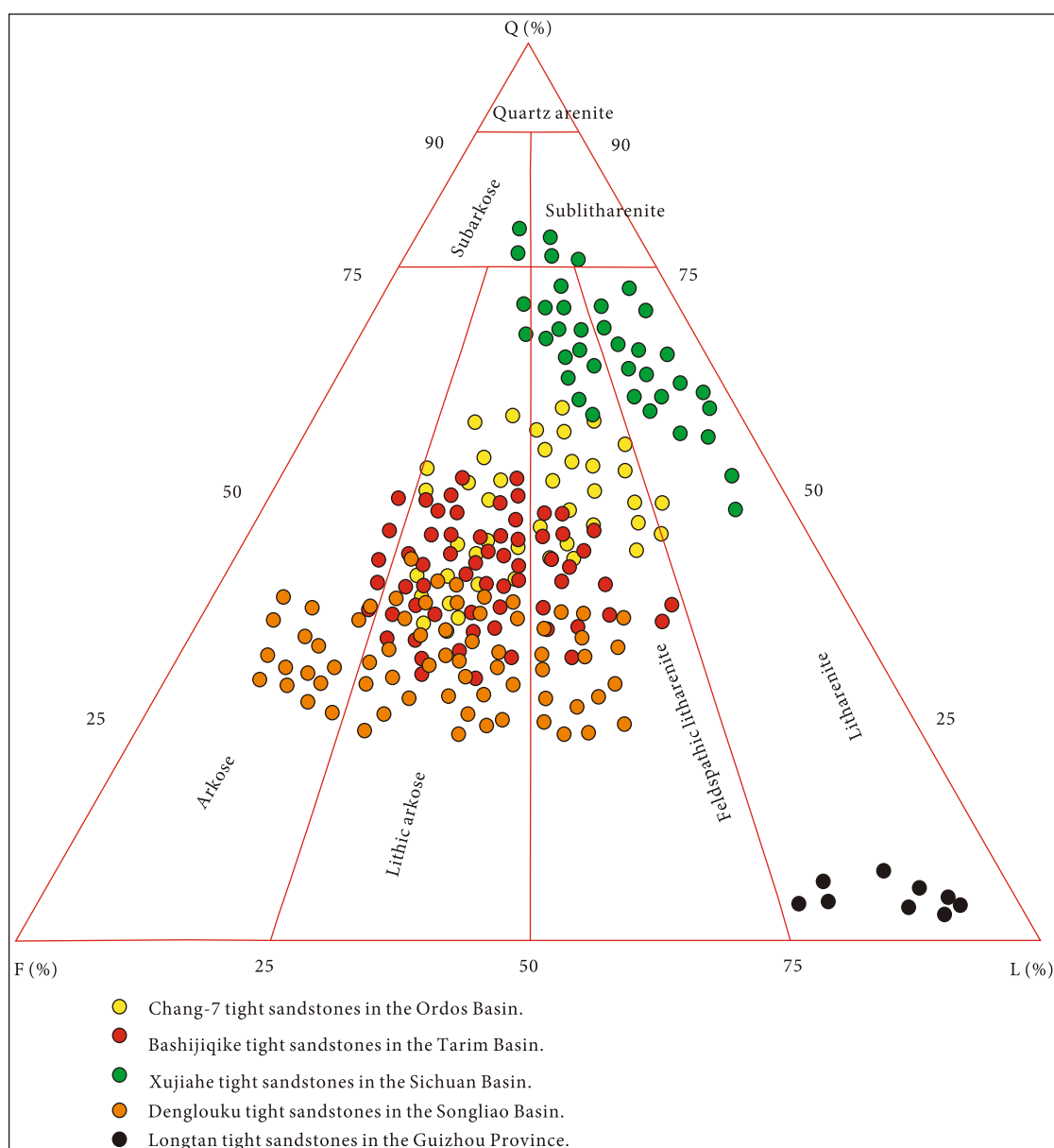
FIGURE 3: A ternary diagram showing the framework-grain composition of typical tight sandstones in China.
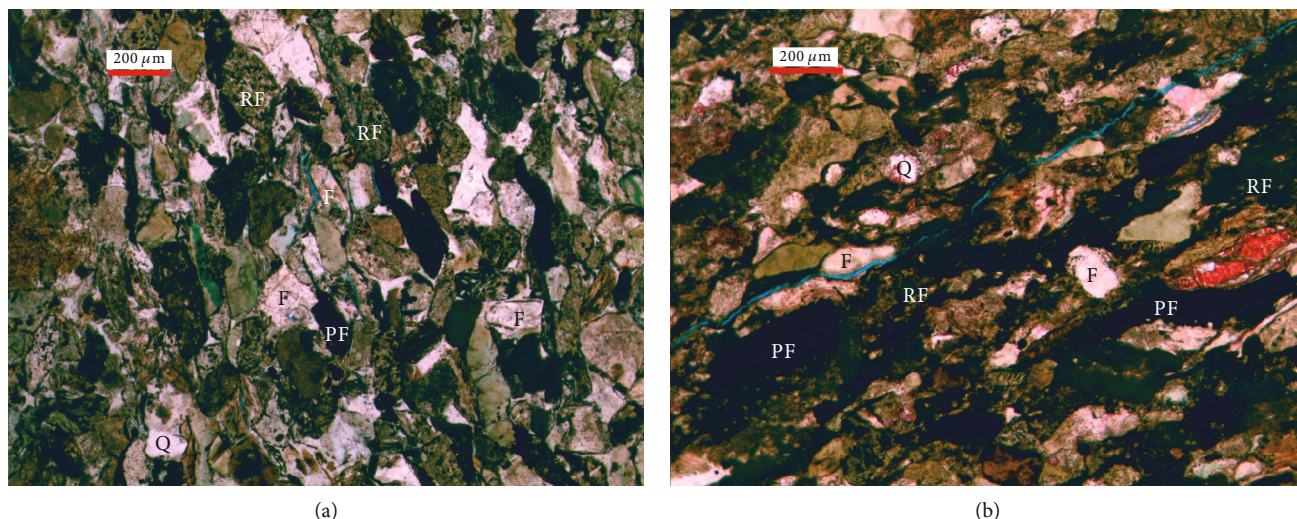
(a)

(b)

Figure 4: Photomicrographs showing mineral composition and texture of the Longtan sandstones. White grains are mostly quartz (Q) and feldspar (F); dark green grains are generally rock fragments (RF); dark blue grains are plant fragments (PF). Pores and microfractures are shown in blue. (a) Litharenite, fine grained, subangular to subrounded, moderate, YV-1-1, 810.85 m, Longtan Formation, and plane-polarized light; (b) litharenite, fine to very fine grained, subangular, moderate sorting to poor sorting, YV-1-3, 681.11 m, Longtan Formation, and plane-polarized light.

carbon contents [30], high thermal maturities, high gas contents, and type III gas-prone organic matter [29, 37], which charged neighboring tight sandstones to form tight gas accumulations. Multiple wells (e.g., the X1 well) have encountered tight gas plays in the Longtan Formation [8, 28], which have raised expectations for tight sand gas in west Guizhou.

3. Data and Analytical Methods

To assess the reservoir features, charging history, and gas source of the Longtan tight sandstones, 11 representative samples from the Longtan Formation were analyzed: 9 sandstone samples, 1 shale sample, and 1 coal sample (Table 1), with depths ranging from 600 to 1500 m. Thin section, SEM, XRD, and fluid inclusion analyses (Table 1) were conducted at Renqiu Jiechuang Petroleum Technology Co., Ltd., and noble gas (Helium and Argon) analyses were completed at the Laboratory of Gas Geochemistry, Lanzhou Institute of Geology, Chinese Academy of Sciences.

Rock property measurements were performed on 1-inch diameter core plugs under the net confining stress of 0.07 Mpa (10 psi) to access the flow capacity (air permeability) and the storage capacity (porosity) of the tight sandstone reservoir.

Thin sections were grinded to a standard of 30-μm thickness to examine the lithology characteristics of the Longtan tight sandstones under the Olympus polarizing optical microscope. All samples were also prepared by vacuum impregnation with blue-dyed resin to facilitate the recognition of porosity. Point-count analysis was performed with respect to detrital framework grains, matrix, cement, interstitial minerals, and porosity, as well as the textural modal grain size and sorting parameters.

SEM imaging was performed by using Tescan VEGA-II to observe the characteristics of the pore networks and types of pore-filling minerals of the tight sandstones. Each sample

was mounted on an aluminum stub and coated with gold/palladium (Au/Pd) alloy before imaging. The temperature and humidity of the experiments were set as 24°C and 35%, respectively.

X-ray diffraction analysis was carried out using D8-Discover to obtain semiquantitative mineralogical data for whole-rock and clay fraction. Samples were first cleaned to avoid any obvious contaminants and then disaggregated in a mortar. According to the Powder Diffraction File provided by the Joint Committee on Power Diffraction-International Center for Diffraction Data, the relative mineral percentages were estimated quantitatively through Rietveld refinement with customized clay mineral structure models [39] at a temperature of 24°C and humidity of 35%.

The fluid inclusion test was performed via microthermometry in accordance with the test method for fluid inclusions in sedimentary basins [40]. The fluid inclusions were observed by using a Leica microscope (DM 4P); the homogenization temperatures were measured by using a cooling-heating stage (LINKAM THMS 600) at a temperature of 20°C and humidity of 30%; and the inclusion compositions were identified by using a microlaser Raman spectrometer (LABH RVIS LabRAM HR 800) at a temperature of 20°C and humidity of 30%.

The noble gas isotope measurements were carried out in accordance with the technique described by Sun [41] for determining noble gas isotopes within natural gas [41]. The samples were first heated to 103°C and then maintained at this temperature for three weeks to remove the adsorbed air inside the samples; then, the samples were placed in an electron bombardment furnace to extract the tight sand gas; the extracted gas samples were heated at 800°C in the sample preparation device by using a titanium sponge to remove hydrocarbon gas, N_2, O_2, CO_2, H_2S, and H_2 and to retain 100% noble gas; and the components of the noble gas isotopes (^3He, ^4He, ^{36}Ar, ^{38}Ar, and ^{40}Ar) were separated
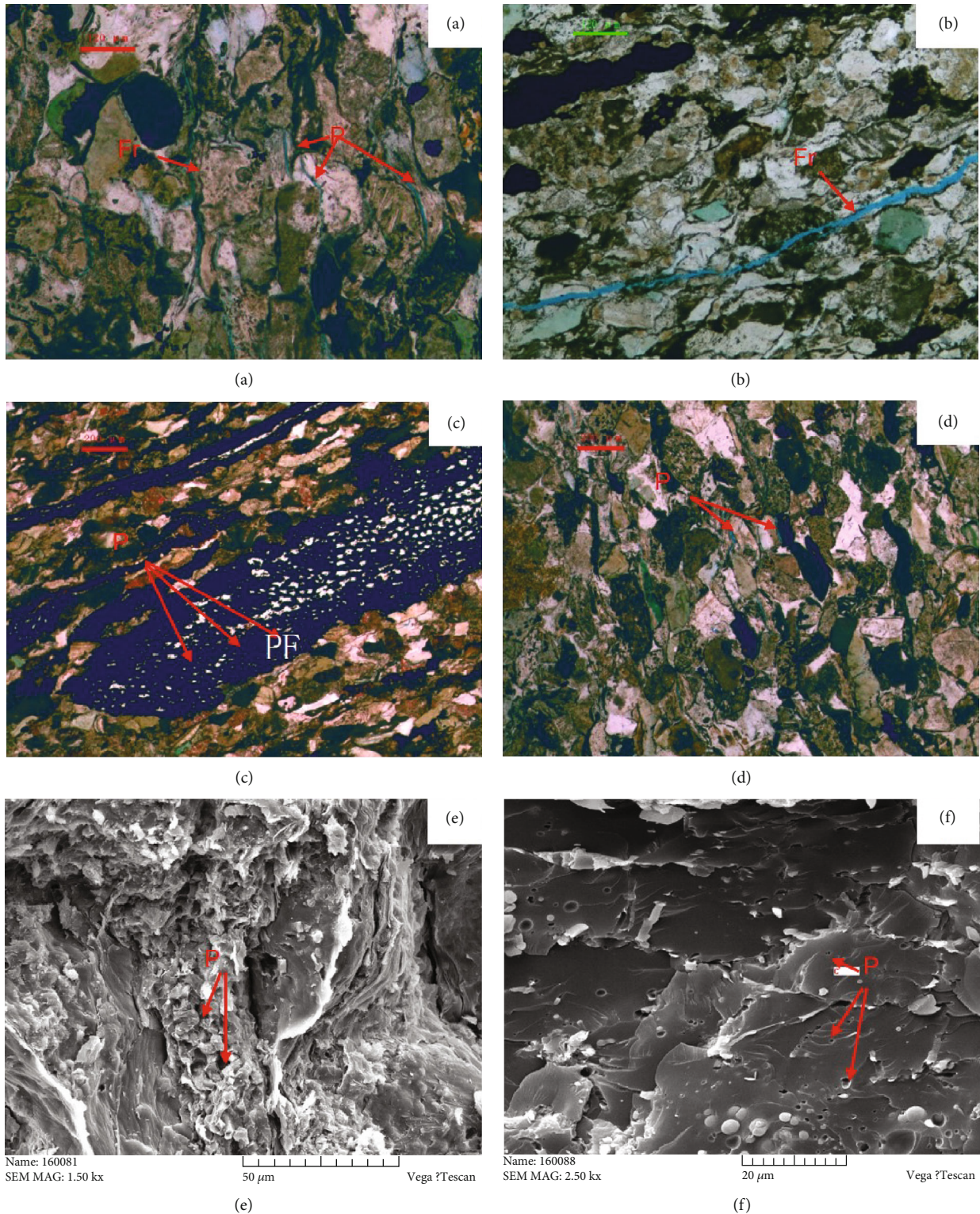
FIGURE 5: Photomicrographs showing pores and microfractures within the Longtan sandstones. (a) Intrapores (*P*) within feldspar and developed microfracture (*Fr*), YV-1-1, 810.85 m, Longtan Formation, and polarized light; (b) a microfracture (*Fr*) is present, HV-3-1, 888.3, Longtan Formation, and polarized light; (c) intergranular micropores (*P*) are observed in plant fragments *(PF)*, YV-1-3, 681.11 m, Longtan Formation, and polarized light; (d) intergranular macropores (*P*) are present within grains, YV-1-1, 810.85 m, Longtan Formation, and polarized light; (e) micropores (*P*) are mainly associated with clay minerals which display fibrous and flake-like structure, YV-1-2, 769.6 m, Longtan Formation, and SEM; (f) organic micropores (*P*) are seen in this sandstone, YV-1-3, 681.11 m, Longtan Formation, and SEM.

TABLE 2: The mineral composition contents of the Longtan sandstone samples in west Guizhou based on X-ray diffraction analysis.

Sample	Clay	Quartz	Orthoclase	Plagioclase	Calcite	Dolomite	Pyrite	Siderite
YV-1-1	59	30		6	3			2
YV-1-2	57	23		17	3			
YV-1-3	56	31		2	8		3	
HV-3-1	67	14		7				12
YV-4	23.9	31.1		4.1	9.1	3	0.2	27.7
Y-28-1	21.2	16.3		0.8	17.7	40.5	3.5	/
Y-28-2	26.8	12		4.5	0.1	55.8	0.8	/
XD-1-1	25.8	12.2		4.8	0.1	56.1	1	/
XD-1-2	46.2	26.7		0.7	9.1	11.4	0.3	5.6

Type: primary
Host mineral: quartz
Shape: oval
Fluid: gas liquid
Size: 10-15 μm

(a)

Type: primary
Host mineral: quartz
Shape: oval
Fluid: gas liquid
Size: 5-20 μm

(b)

Type: secondary
Host mineral: quartz
Shape: oval
Fluid: brine
Size: 1-5 μm

(c)

Type: secondary
Host mineral: quartz
Shape: oval
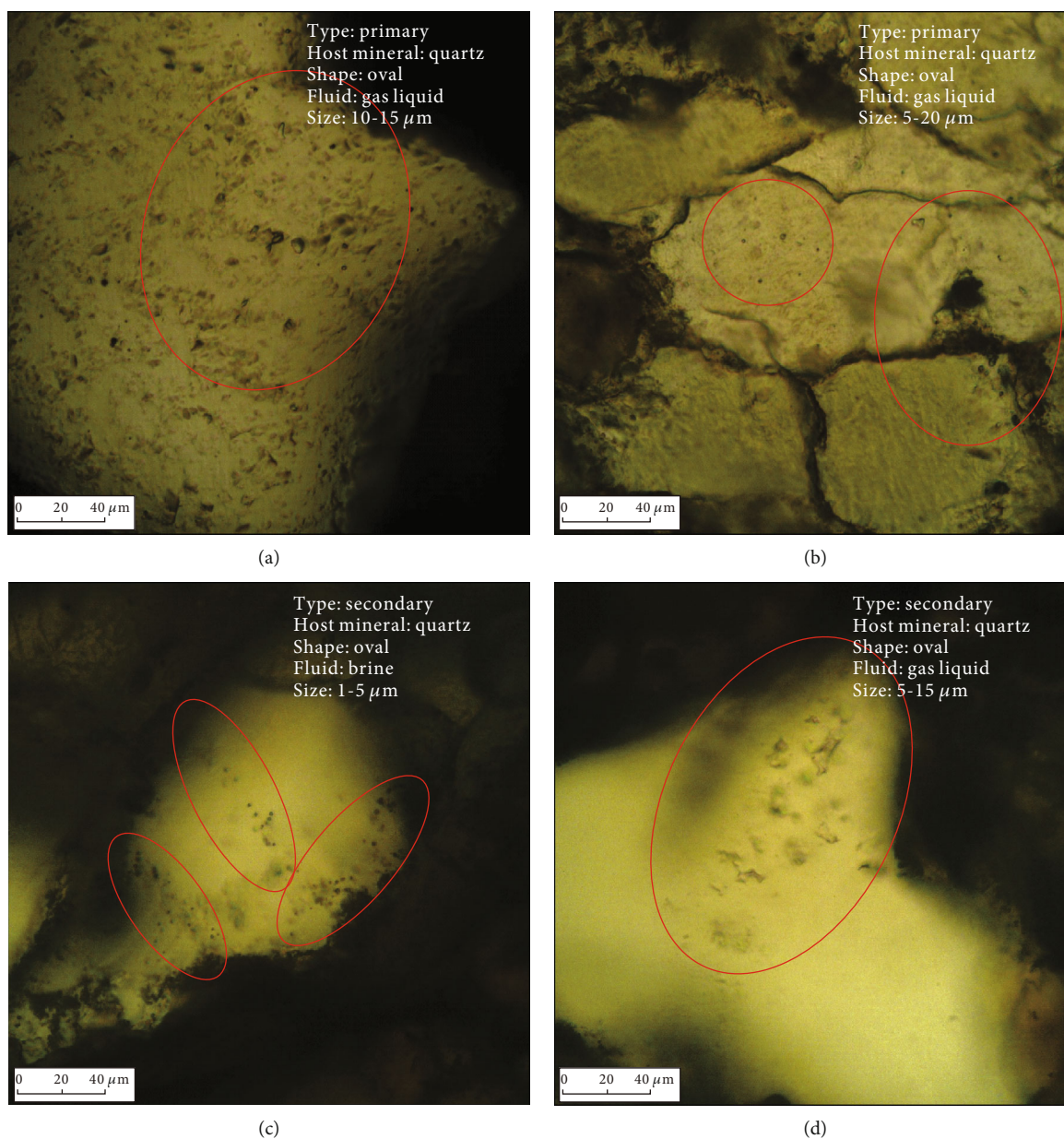Fluid: gas liquid
Size: 5-15 μm

(d)

FIGURE 6: Characteristics of the typical fluid inclusions within the Longtan tight sandstones in west Guizhou: (a) primary gas-liquid inclusion under polarized light for the YV-1-1 sample; (b) primary gas-liquid inclusion under polarized light for the YV-1-3 sample; (c) secondary brine inclusion under polarized light for the HV-3-1 sample; and (d) secondary gas-liquid inclusion under polarized light for the HV-3-1 sample.

TABLE 3: Characteristic parameters of the fluid inclusions within the Longtan tight sandstones in west Guizhou.

Sample	Genetic type	Host mineral	Shape	Size (μm)	Fluid type	Gas-liquid ratio (%)	Homogenization temperature (°C)
YV-1-1	Primary	Quartz	Oval	5-10	Gas-liquid	10	109
YV-1-1	Primary	Quartz	Oval	5-10	Gas-liquid	10	116
YV-1-1	Primary	Quartz	Oval	10-15	Gas-liquid	10	124
YV-1-1	Primary	Quartz	Oval	10-15	Gas-liquid	10	136
YV-1-1	Primary	Quartz	Oval	5-15	Gas-liquid	10	128
YV-1-1	Primary	Quartz	Oval	5-20	Gas-liquid	10	131
YV-1-2	Primary	Quartz	Oval	10-15	Gas-liquid	10	112
YV-1-2	Primary	Quartz	Oval	18	Gas-liquid	10	135
YV-1-2	Primary	Quartz	Oval	5-10	Gas-liquid	10	124
YV-1-2	Primary	Quartz	Oval	5-20	Gas-liquid	10	126
YV-1-2	Primary	Quartz	Oval	5-15	Gas-liquid	10	110
YV-1-2	Primary	Quartz	Oval	5-10	Gas-liquid	10	132
YV-1-3	Primary	Quartz	Oval	5-20	Gas-liquid	10	115
YV-1-3	Primary	Quartz	Oval	5-10	Gas-liquid	10	120
YV-1-3	Primary	Quartz	Oval	10-15	Gas-liquid	10	125
YV-1-3	Primary	Quartz	Oval	5-20	Gas-liquid	10	116
YV-1-3	Primary	Quartz	Oval	10-15	Gas-liquid	10	130
YV-1-3	Primary	Quartz	Oval	10-15	Gas-liquid	10	127
HV-3-1	Secondary	Quartz	Oval	1-5	Brine	0	/
HV-3-1	Secondary	Quartz	Oval	1-5	Brine	0	/
HV-3-1	Secondary	Quartz	Oval	5-15	Gas-liquid	25	124
HV-3-1	Secondary	Quartz	Oval	1-5	Brine	0	/

according to their boiling points by using cryogenic pumps, activated carbon furnaces, and liquid nitrogen. Finally, the contents of the noble gas isotopes were determined by using a mass spectrometer (VG 5400 MS).

4. Results

4.1. Reservoir Characteristics. The results of thin section analysis show that the Longtan tight sandstones are classified as litharenites according to the classification scheme recommended by Folk [42]. The dominant compositions of the Longtan sandstones are the lithic rock fragments whose contents are greater than 70% (Figure 3). Detailed studies further demonstrate that the lithic rock fragments are primarily made of mud clasts ranging from 48 to 50% and minor volcanic, metamorphic, sedimentary, tuff, and mica rock fragments based on the observations of thin sections. These mud clasts were generally formed in marine-continental environments [43]. Interstitial material includes matrix with an average content of 7% and cement with an average content of 10% dominated by clay minerals. The grain sizes are mostly very fine to fine sands, exhibiting moderate sorting and low (subangular) to moderate (subrounded) sphericity (Figures 4(a) and 4(b)). Overall, the Longtan sandstones have low compositional and textural maturities.

The term "micropore" in tight sandstones is generally used to describe pore sizes<10 μm and "micropore throats" to describe pore throat sizes<1 μm [44]. The Longtan sandstones are distinguished petrographically from conventional

sandstones by the extensive existence of micropores (Figures 5(c), 5(e), and 5(f)) and the presence of microfractures (Figures 5(a) and 5(b)). The intergranular and intragranular macropores, however, are rare in the Longtan sandstones (Figures 5(a)–5(d)). Micropores are pervasive owing to high clay contents (Table 2). The clay minerals (e.g., mixed layer illite/smectite) display fibrous, flake-like, and honeycomb-like morphology (Figure 5(e)) and have a negative effect on reservoir properties of sandstones [45]. Micropores within organic matter have also been observed (Figure 5(f)). The micropores associated with authigenic clays are treated as dead end pores and have no positive contribution to the fluid flow.

4.2. Fluid Inclusions Characteristics. The Longtan tight sandstones are characterized by low porosities and permeabilities with the existence of micropores and microfractures. The results of fluid inclusion analysis show that the fluid inclusions are mostly located in the microfractures of quartz minerals and hardly observed in cements (Figure 6). Overall, the fluid inclusions have low abundance and are mainly divided into three types: primary gas-liquid inclusions, secondary brine inclusions, and secondary gas-liquid inclusions (Figure 6). The original gas-liquid inclusions of the YV-1-1 and YV-1-3 samples are scattered and disordered (Figures 6(a) and 6(b)) and are mainly located in quartz minerals with a wide range of sizes (5-20 μm). The original gas-liquid inclusion shapes are oval, and their liquid ratios are approximately 10% (Table 3). The secondary inclusions
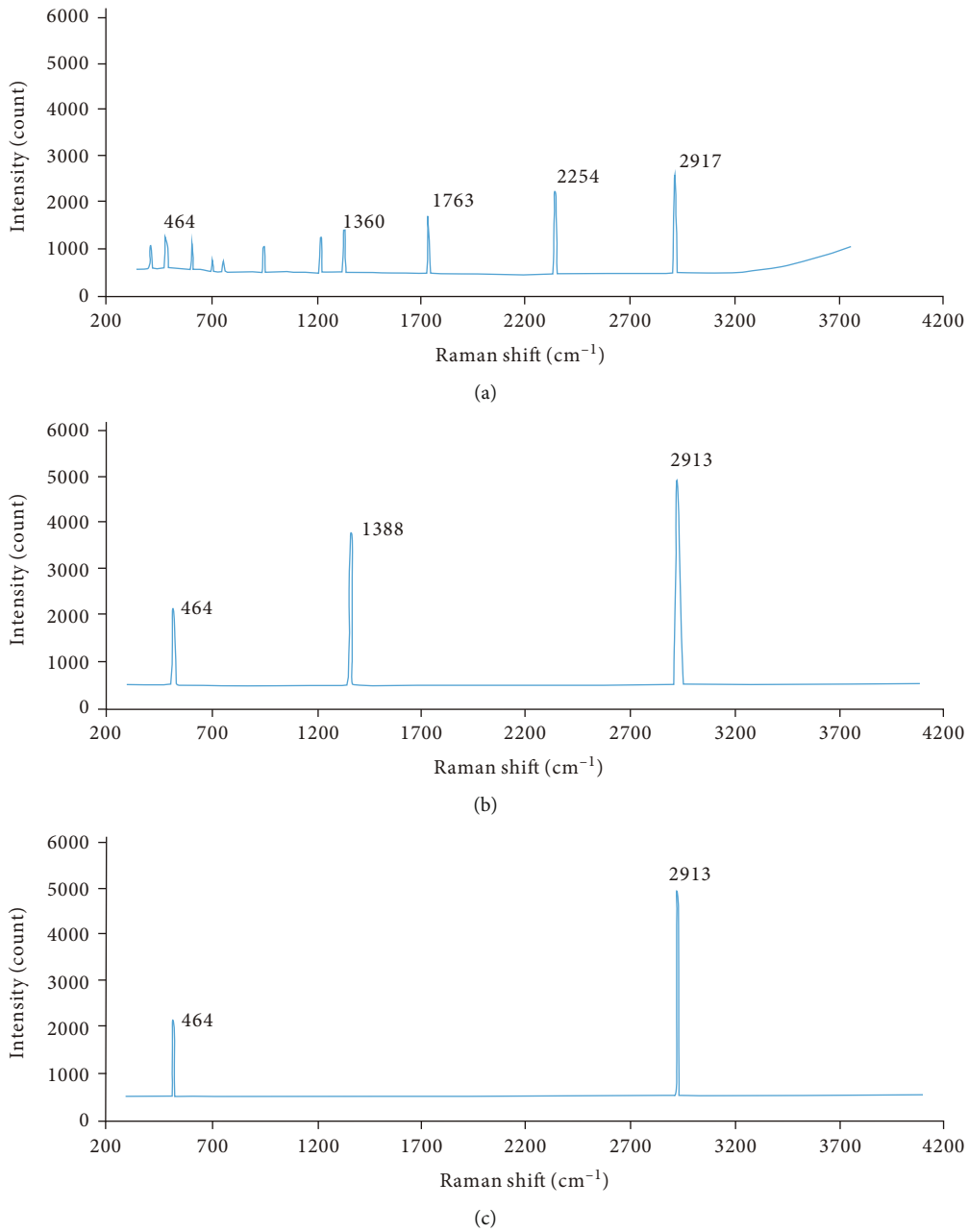
(a)

(b)

(c)

Figure 7: Characteristics of laser Raman spectra of the fluid inclusions within the Longtan tight sandstones in west Guizhou: (a) saturated hydrocarbon; (b) $CH_4 + CO_2$; (c) CH_4.
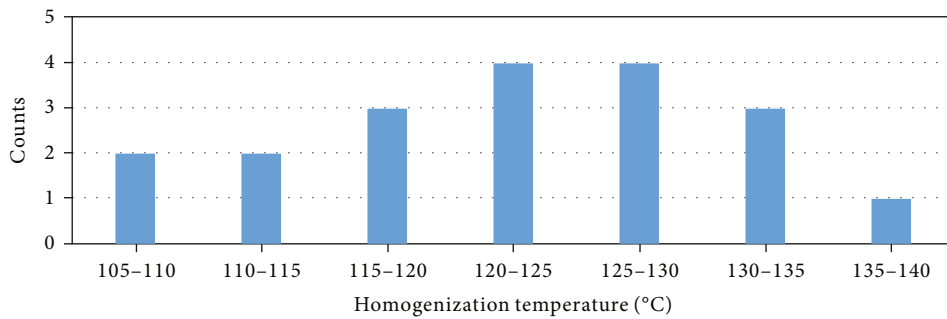

Figure 8: Histogram of homogenization temperatures of the fluid inclusions within the Longtan tight sandstones in west Guizhou.

TABLE 4: Contents and ratios of helium and argon isotopes within the air and Longtan tight sand gas in west Guizhou.

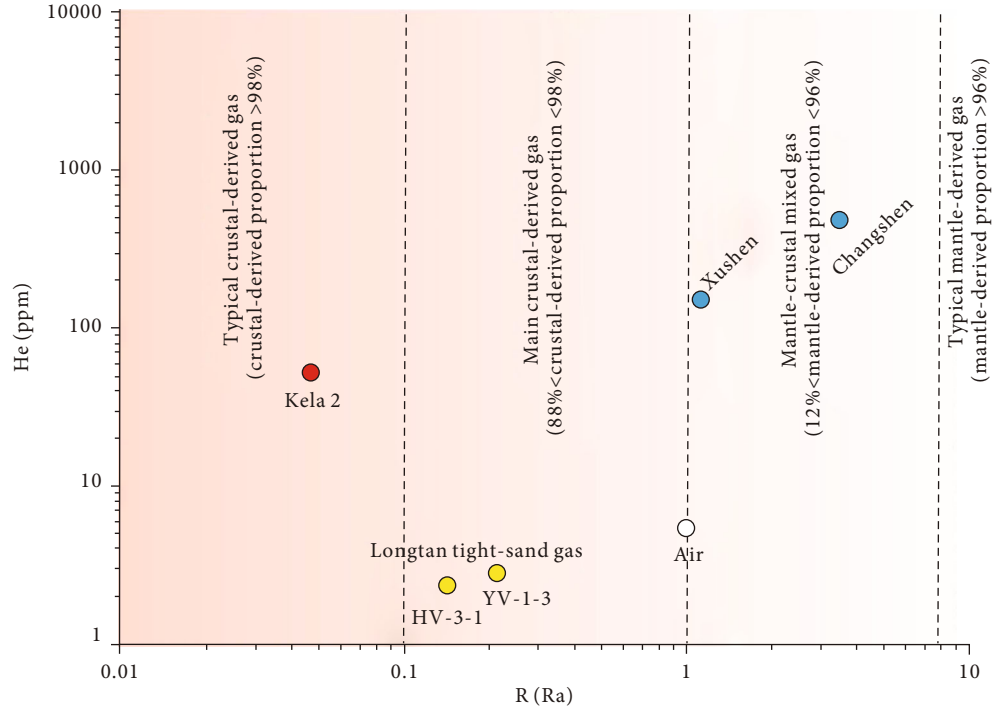| Sample	He (mL/g)	Ar (mL/g)	R/Ra	^{3}He/^{4}He	^{4}He/^{20}Ne	^{40}Ar/^{36}Ar	^{38}Ar/^{36}Ar
YV-1-3	2.91×10^{-6}	9.72×10^{-6}	0.22	3.08×10^{-7}	29	924	0.188
HV-3-1	2.45×10^{-6}	9.95×10^{-6}	0.16	2.30×10^{-7}	25	1539	0.187
Air	5.24×10^{-6}	9340×10^{-6}	1	1.40×10^{-6}	0.288	295.5	0.188

FIGURE 9: Crossplots of R/Ra versus He concentration of typical gas fields in China and Longtan tight sand gas in west Guizhou, showing that the Longtan R/Ra values are in the range of values for main crustal-derived gas. The data of Kela2, Xushen, and Changshen are from Wang et al. [50].

of the HV-3-1 sample are grouped and clustered (Figures 6(c) and 6(d)) and are mainly located in microfractures within quartz minerals and have a very wide range of sizes (1–15 μm). The shapes of the secondary inclusions are mainly oval (Table 3). The gas-liquid ratio of the secondary gas-liquid inclusions of the HV-3-1 sample is 25% (Table 3), and they are characterized by observing a brown fluorescence. Laser Raman spectra of the secondary gas-liquid inclusions have shown that the fluid compositions of some inclusions are rich in saturated hydrocarbons (Figure 7(a)); some inclusions mainly contain methane with low contents of carbon dioxide (Figure 7(b)); and other inclusions are rich in methane (Figure 7(c)). As a result, according to the distributions, colors, and compositions of the inclusions, the secondary gas-liquid inclusions within the Longtan sandstones are mainly hydrocarbon fluids captured during the sandstone diagenesis stage.

The homogenization temperatures of the hydrocarbon-rich gas-liquid inclusions can reflect the paleotemperatures of when hydrocarbons are captured [22]. The homogenization temperature results of the gas-liquid inclusions within the Longtan sandstones (Figure 8) show that the homogeni-

zation temperatures of the inclusions range from 105°C to 140°C and present a unimodal distribution with a single peak at 120°C–130°C, indicating that the charging processes of oil and gas within the Longtan sandstones were continuous.

4.3. Compositions of the Noble Gas Isotopes. The results of the noble gas isotopic analysis within the Longtan tight sand gas samples show that the contents of helium (He) are 2.91×10^{-6} mL/g and 2.45×10^{-6} mL/g, respectively, which are lower than that in the atmosphere at 5.24×10^{-6} mL/g; the contents of argon (Ar) are 9.72×10^{-6} mL/g and 9.95×10^{-6} mL/g, respectively, which are 3 orders of magnitude lower than that in the atmosphere at 9340×10^{-6} mL/g; the ^{3}He/^{4}He values are 3.08×10^{-7} and 2.30×10^{-7}, respectively, which are lower than that in the atmosphere of 1.4×10^{-6}; the ^{4}He/^{20}Ne values are 29 and 25, respectively, which are approximately 2 orders of magnitude greater than that in the atmosphere at 0.288; the ^{40}Ar/^{36}Ar values are 924 and 1539, respectively, which are greater than that in the atmosphere at 295.5; and the ^{38}Ar/^{36}Ar values are 0.188 and
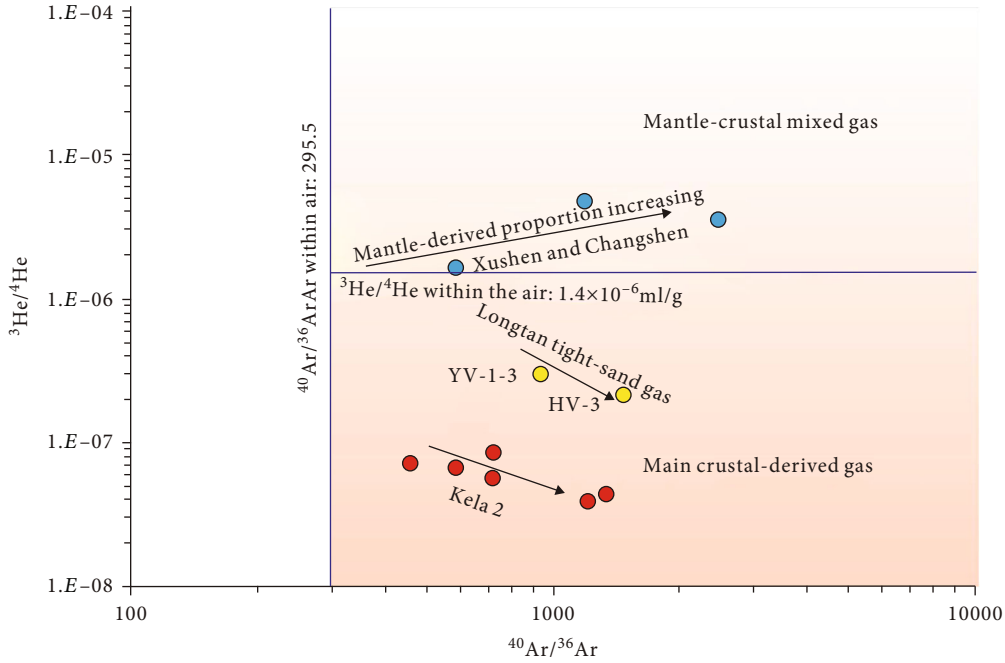
FIGURE 10: Crossplots of $^{40}Ar/^{36}Ar$ versus $^{3}He/^{4}He$ of typical gas fields in China and Longtan tight sand gas in west Guizhou, showing that the Longtan $^{40}Ar/^{36}Ar$ values decrease with $^{3}He/^{4}He$ values. The data of Kela2, Xushen, and Changshen are from Wang et al. [50].

0.187, respectively, which are close to that in the air at 0.188 (Table 4). The drastic differences in the isotopic ratios (e.g., $^{4}He/^{20}Ne$) among the samples and the air indicates that the compositions of tight gas samples are hardly influenced by those isotopic ratios in the air.

Stable isotopes of He include ^{3}He and ^{4}He, where ^{3}He is a primordial nuclide, and ^{4}He is a radioactive nuclide [46]. The $^{3}He/^{4}He$ values in air, mantle-derived gas, and crust-derived gas are approximately 1.4×10^{-6}, 1.0×10^{-5}, and 1.0×10^{-8}, respectively [47, 48]. He isotopes within tight sand gas originate from air, mantle, and crust. Their relative contents determine the $^{3}He/^{4}He$ values within the Longtan tight sand gas. The $^{3}He/^{4}He$ values (Table 4) within the Longtan tight sand gas samples are much smaller than those in the air and mantle-derived gas, indicating that the He isotopes within the samples are mainly crust-derived. In addition, researchers have demonstrated that the $^{3}He/^{4}He$ ratio of the sample (R) to the atmospheric $^{3}He/^{4}He$ ratio (Ra) can effectively represent the gas origin in the sample (Figure 9). The R/Ra values of crust-derived gas range from 0.01 to 0.1 and those of mantle-derived gas are greater than 8 [47, 49, 50]. The R/Ra values of the Longtan samples are slightly greater than 0.1 (Table 4), which indicates that the He isotopes are primarily crust-derived with a small contribution from mantle-derived helium (Figure 9). According to Equation (1) [51] the proportions of mantle-derived helium within the tight sand gas samples of the Longtan Formation are 2.2% and 3.0%, respectively.

$$R_{Mantle} = \frac{\left(^{3}He/^{4}He\right)_{Sample} - \left(^{3}He/^{4}He\right)_{Crust}}{\left(^{3}He/^{4}He\right)_{Mantle} - \left(^{3}He/^{4}He\right)_{Crust}} \times 100\%, \quad (1)$$

where R_{Mantle} is the proportion of mantle-derived He, $(^{3}He/^{4}He)_{Sample}$ is the $^{3}He/^{4}He$ value of the sample, $(^{3}He/^{4}He)_{Crust}$ is the crust-derived $^{3}He/^{4}He$ value, and $(^{3}He/^{4}He)_{Mantle}$ is the mantle-derived $^{3}He/^{4}He$ value.

Stable isotopes of Ar include ^{36}Ar, ^{38}Ar, and ^{40}Ar, where ^{36}Ar and ^{38}Ar are primordial nuclides and ^{40}Ar is a radioactive nuclide that is produced by the decay of potassium (K) [52]. The ^{40}Ar contents are highly dependent on the K content and decay time [21]. There is a wide range of crust-derived and mantle-derived $^{40}Ar/^{36}Ar$ values, and they cannot be used to differentiate the gas origin of Ar. However, a couple studies show that the crust-derived $^{40}Ar/^{36}Ar$ values decrease as the $^{3}He/^{4}He$ values increase (e.g., the Kela2 gas field), and the mantle-derived $^{40}Ar/^{36}Ar$ values show the opposite trend (e.g., the Xushen and Changshen gas fields). The $^{40}Ar/^{36}Ar$ values of the Longtan tight sand gas samples behave the crustal-derived feature (Figure 10). This indicates that Longtan Ar has a crustal origin, which is consistent with the results from the $^{3}He/^{4}He$ analysis.

5. Discussion

5.1. Charging History. The integration of homogenization temperatures of fluid inclusions and burial and thermal histories are important for assessing the period and timing of hydrocarbon charging into the reservoir [14, 15, 17, 22]. PetroMod was used to generate the burial and thermal histories of the YV-1 and HV-3 wells (Figure 11), which are based on thermal maturity (Ro) data and the pioneering studies of Dou et al. [31] and Wang et al. [53]. The results of the burial and thermal histories (Figure 11) of the study area show that the paleowater depth of the LV-1 and HV-3 well areas in west Guizhou gradually increased from the Late Permian
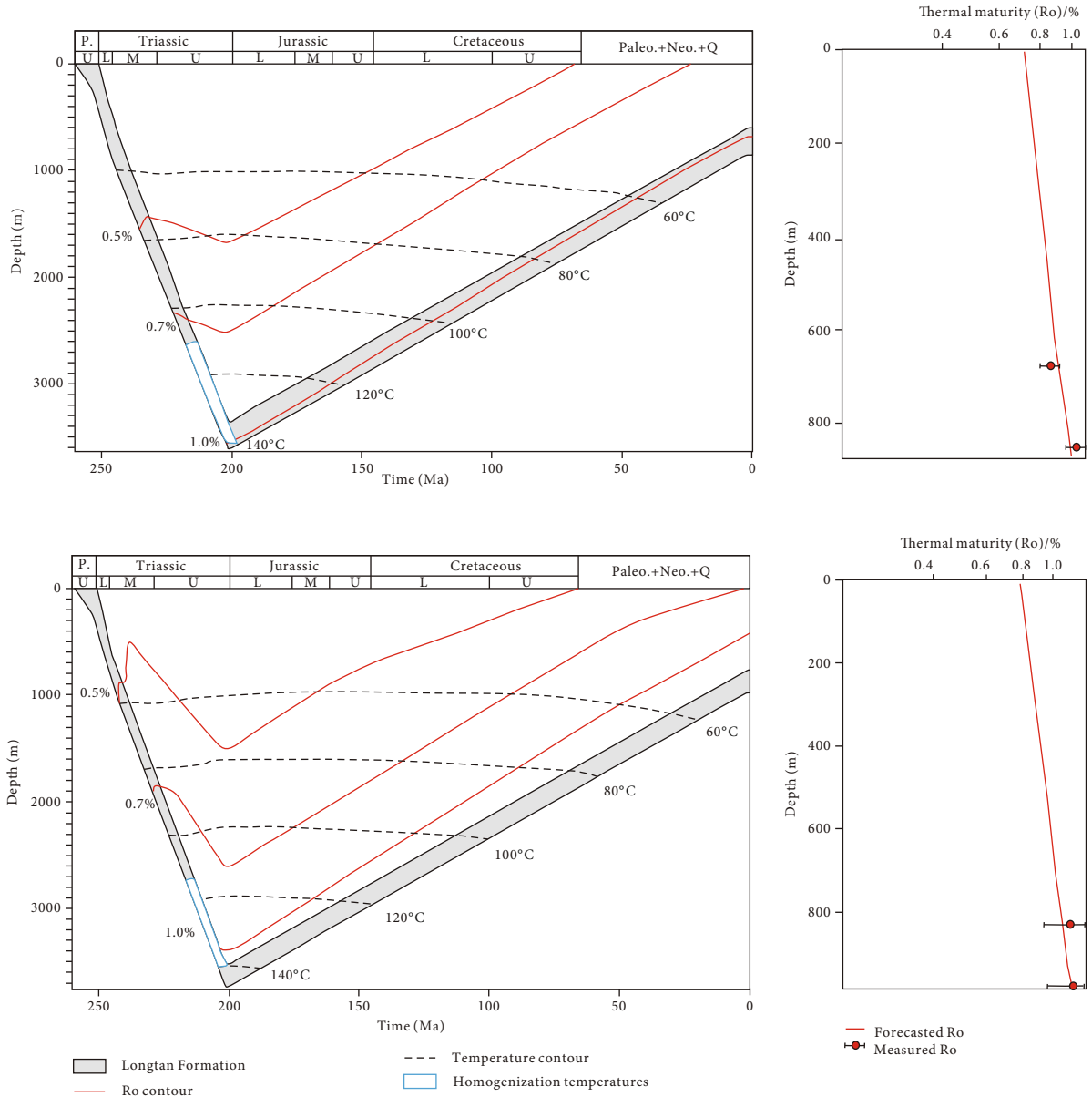
FIGURE 11: Burial and thermal histories of the Longtan Formation in the study area in west Guizhou: (a) YV-1 and (b) HV-3. The results show that the Ro values of YV-1 and HV-3 reached above 1.0% during the Late Triassic, and the forecasted Ro values match the measured Ro values at the YV-1 and HV-3 wells.

TABLE 5: Potassium contents of coals and shales.

Lithology	Place and time	Average K content (%)
Shale	Shales in large basins around the world [55]	3.24
Shale	27 shales in China [55]	2.67
Shale	2 shales in the Jurassic in the Tarim Basin [21]	2.64
Shale	Shales in the Permian in the Sichuan Basin [51]	0.86
Coal	Coals in China [56]	0.214

to the Middle-Late Triassic, and the sedimentary environments transferred from marine-continental transitional settings to marine carbonate depositions [53]. The burial depth of the Longtan Formation gradually increased, the

thermal maturity of organic matter increased, and Ro reached approximately 1.3% in the Late Triassic. After that, multiple stages of tectonic movements (e.g., the Indosinian, Yanshanian, and Himalayan) resulted in uplift with intense
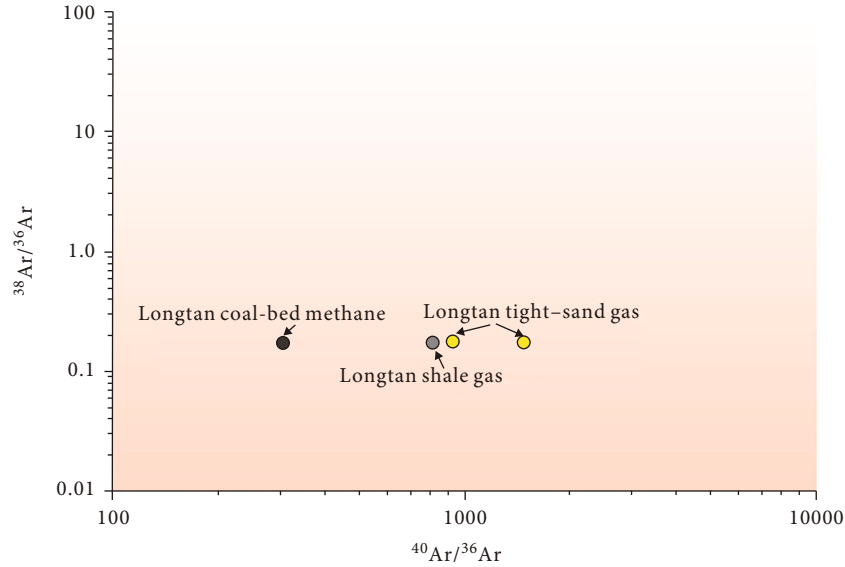
FIGURE 12: Crossplots of $^{40}Ar/^{36}Ar$ versus $^{38}Ar/^{36}Ar$ of gases within the Longtan tight sandstones, shales, and coals in west Guizhou, showing that $^{40}Ar/^{36}Ar$ values of the Longtan shale and tight sand gas are close in value, $^{40}Ar/^{36}Ar$ values of the Longtan coal and tight sand gas differ significantly in value, and the $^{38}Ar/^{36}Ar$ values of the Longtan shale, coal, and tight sand gas are very close in value.

TABLE 6: Forecasted and measured $^{40}Ar/^{36}Ar$ ratios of shales and coal seams in the Longtan Formation in west Guizhou.

Source rock lithology	Forecasted $^{40}Ar/^{36}Ar$	Measured $^{40}Ar/^{36}Ar$
Shale	928.00	816.00
Coal	346.00	308.00
Shale/coal	2.68	2.65

faulting, fracturing, and folding, and the thermal evolution of organic matter in the Longtan Formation ceased (Figure 11). Until the Quaternary, thin layer residues and slope deposits were formed, and the burial depth and thermal maturity of the Longtan Formation slightly increased (Figure 11).

The homogenization temperatures outlined above for the gas-liquid inclusions within the Longtan tight sandstones range from 105°C to 140°C and show that the Longtan tight sand gas is a single-stage accumulation. Based on the thermal histories of the study area, the main charging time of the tight sand gas in the Longtan Formation occurred in the Late Triassic (215–205 Ma).

5.2. Tight Sand Gas Source. The ^{40}Ar contents within the gas samples are determined by the amount of Potassium (K) contained in the gas source rocks of the same period. The K contents in shales and coals show a large difference (Table 5), which provides a basis for using $^{40}Ar/^{36}Ar$ to calculate the source rock (e.g., shales and coals) contribution of tight sand gas [21, 54]. Potassium sources of ^{40}Ar within the tight sand gas include detrital minerals, mantle, air, and source rocks (shales and coals). Potassium in detrital minerals is mainly present in potassium feldspars (orthoclases). According to X-ray diffraction analysis, the mineral compositions of the Longtan tight sandstone are mainly clay min-

erals and quartzes and do not consist of potassium feldspars (Table 2). Therefore, ^{40}Ar contents within the Longtan tight sand gas includes no contribution from the detrital minerals. According to the results discussed above, ^{40}Ar within the Longtan tight gas is mainly crust-derived; thus, the mantle contribution is negligible. Therefore, the calculation model of the shale and coal contribution for the Longtan tight sand gas was established based on the pioneering studies of Kaneoka and Takaoka [18], Ballentine et al. [24], Zhang et al. [21], and Liu et al. [9]. First, the $^{40}Ar/^{36}Ar$ values and K contents of source rocks at the same age show a positive correlation, and the $^{40}Ar/^{36}Ar$ values of the Longtan coals can be calculated under the circumstance of determining the $^{40}Ar/^{36}Ar$ values of the Longtan shales and the K contents of the Longtan coals and shales via Equation (2) [21]. The potassium contents of the Longtan shales are set as the average K content (2.67%) of shales in China (Table 5); the contents of potassium in the coal seam are based on the average content (0.214%) of coals in China (Table 5); the $^{40}Ar/^{36}Ar$ values of the Permian shale range from 592 to 1672 [54], and the $^{40}Ar/^{36}Ar$ values of the Longtan coals are set as the average $^{40}Ar/^{36}Ar$ value (928) of the Permian shale; then, the $^{40}Ar/^{36}Ar$ value of the Longtan coals is calculated as 346. Second, the shale-derived and coal-derived contributions for the Longtan tight sand gas can be calculated under the circumstance of determining the $^{40}Ar/^{36}Ar$ values of the Longtan tight gas samples, shales, and coals by using Equations (3) and (4), respectively. The shale-derived contributions for the Longtan tight sand gas in the YV-1-3 and HV-3-1 samples are 99% and 100%, respectively, which indicates that a very small proportion of the Longtan coalbed methanes were charged into the Longtan tight sand reservoir. Furthermore, the $^{40}Ar/^{36}Ar$ values within the Longtan tight gas are very close to the measured $^{40}Ar/^{36}Ar$ value of the Longtan shale sample and differ
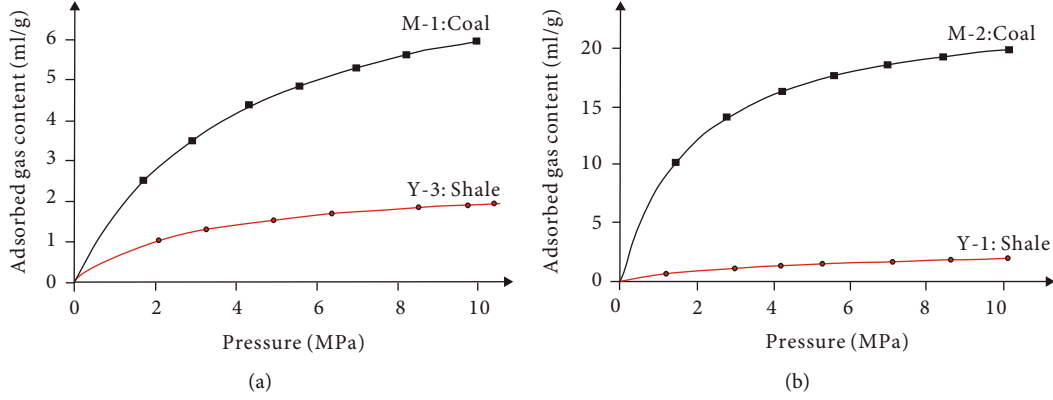
FIGURE 13: Adsorption capacity comparison between shales and coals: (a) M-1, coal, $R_o = 0.56\%$ and Y-3, $R_o = 0.58\%$, shale; and (b) M-2, coal, $R_o = 1.51\%$ and Y-1, $R_o = 1.57\%$, shale (modified from Xia et al. [62]). The results show that the adsorption capacity of shales is greater than that of coals at a given maturity and pressure.

significantly from the measured $^{40}Ar/^{36}Ar$ value of the Longtan coal sample (Figure 12), which indicates that the Longtan tight sand gas mainly originates from the Longtan shales. This understanding, in addition to the results from the calculation model, signifies that the Longtan shales are the main source rocks that can generate gas to charge the tight sandstones to form tight gas accumulations in the Longtan Formation. As a result, the measured $^{40}Ar/^{36}Ar$ values of the Longtan shales and coals are consistent with the forecasted $^{40}Ar/^{36}Ar$ values from the calculation model (Table 6), demonstrating that the model is viable to calculate the source rock contribution to the tight sand gas.

$$\frac{K_{\text{Shale}}}{K_{\text{Coal}}} = \frac{\left(^{40}Ar/^{36}Ar\right)_{\text{Shale}} - \left(^{40}Ar/^{36}Ar\right)_{\text{Air}}}{\left(^{40}Ar/^{36}Ar\right)_{\text{Coal}} - \left(^{40}Ar/^{36}Ar\right)_{\text{Air}}}, \qquad (2)$$

where K_{Shale} is the K content within the Longtan shale; K_{Coal} is the K content within the Longtan coal; $\left(^{40}Ar/^{36}Ar\right)_{\text{Shale}}$ is the $^{40}Ar/^{36}Ar$ value of the Longtan shale; $\left(^{40}Ar/^{36}Ar\right)_{\text{Air}}$ is the $^{40}Ar/^{36}Ar$ value of air; and $\left(^{40}Ar/^{36}Ar\right)_{\text{Coal}}$ is the $^{40}Ar/^{36}Ar$ value of the Longtan coal.

$$R_{\text{Shale}} = \frac{\left[\left(^{40}Ar/^{36}Ar\right)_{\text{Sample}} - \left(^{40}Ar/^{36}Ar\right)_{\text{Air}}\right] - \left[\left(^{40}Ar/^{36}Ar\right)_{\text{Coal}} - \left(^{40}Ar/^{36}Ar\right)_{\text{Air}}\right]}{\left[\left(^{40}Ar/^{36}Ar\right)_{\text{Shale}} - \left(^{40}Ar/^{36}Ar\right)_{\text{Air}}\right] - \left[\left(^{40}Ar/^{36}Ar\right)_{\text{Coal}} - \left(^{40}Ar/^{36}Ar\right)_{\text{Air}}\right]}, \qquad (3)$$

where R_{Shale} is the shale-derived contribution for tight sand gas; $\left(^{40}Ar/^{36}Ar\right)_{\text{Sample}}$ is the $^{40}Ar/^{36}Ar$ value of the sample; $\left(^{40}Ar/^{36}Ar\right)_{\text{Air}}$ is the $^{40}Ar/^{36}Ar$ value of air; $\left(^{40}Ar/^{36}Ar\right)_{\text{Shale}}$ is the $^{40}Ar/^{36}Ar$ value of the Longtan shale; and $\left(^{40}Ar/^{36}Ar\right)_{\text{Coal}}$ is the $^{40}Ar/^{36}Ar$ value of the Longtan coal.

$$R_{\text{Coal}} = 1 - R_{\text{Shale}}, \qquad (4)$$

where R_{coal} is the coal-derived contribution for tight sand gas and R_{Shale} is the shale-derived contribution for the tight sand gas.

The gas expulsion capacity from an organic-rich shale or coal is controlled by both gas generation and adsorption capacity [57–59]. The gas generation capacity is determined by the thickness, type, richness, and maturity of organic matter [34, 60]. The YV-1 and HV-3 wells featured thick organic-rich shales that were 49.8 and 54.3 m, greater than those of the coals, but the maturity and richness are almost the same, and therefore, the gas generation capacity of shales at the YV-1 and HV-3 wells is greater than that of coals in west Guizhou. The adsorption capacity is determined by kerogen type, richness, maturity, mineral composition, pore structure, temperature, and pressure [59, 61]. Xia et al. [62] showed that the adsorption capacity of coals is much greater than that of shales (Figure 13), mainly owing to the differences in chemical structures, maceral composition, and pore structure [62, 63]. During burial history, maturities of organic matter increase with depth, and the generation of gas from source rock begins at levels of thermal maturity greater than 0.6% R_o [64]. The generation of gas was first stored in source rocks and started to migrate into reservoirs after full saturation within the source rocks [57]. Therefore, the gas expulsion capacity of shales the YV-1 and HV-3 wells is speculated to be greater than that of coals, and the shale contribution to the tight sand gas is prevailing, which is consistent with the result from the calculation model. Uncertainty exists in the calculation model due to the limitation of the number of tight gas samples in west Guizhou. The calculation model from He and Ar isotopes should be optimized with the acquisition of more gas samples, and integration of source rock thickness, richness, maturity, and burial history, etc. to understand hydrocarbon generation and expulsion characteristics are import for assessing the result of the calculation model.

6. Conclusions

Sandstones, shales, and coal seams are interbedded in the Longtan Formation in marine-continental transitional environments of coal measures, and the potential of the tight sand gas are unclear. This paper analyzes the reservoir characteristics, charging history, and source rock contribution for the Longtan tight sand gas in west Guizhou, and the following conclusions can be drawn.

(1) The Longtan sandstones in this study are classified as litharenites which are characterized by low compositional and textural maturities, and high clay contents. The clay minerals are dominated by illite/smectite (I/S) mixed layers. High clay contents are one of the key factors leading to the poor reservoir quality of the Longtan sandstones

(2) Constrained from homogenization temperatures of the gas-liquid inclusions and burial and thermal histories, the main charging time of the tight sand gas in the Longtan Formation occurred in the Late Triassic (215–205 Ma). The helium and argon isotope analysis of the Longtan tight sand gas shows that the tight sand gas is primarily crust-derived with a very low content of mantle-derived gas. The occurrences of gas charge into the Longtan sandstones indicate the potential for tight gas development in West Guizhou

(3) The calculation model of the shale and coal contribution for the Longtan tight sand gas was established. The results of calculation model and expulsion capacity show that the main source rocks of the Longtan tight sand gas are the Longtan shales; thus, the coal-derived contribution for tight sand gas in the Longtan Formation is minor, signifying that the Longtan shales are the key contributors for tight gas in the Longtan Formation

Data Availability

The data used to support the findings of this study are included within the article.

Conflicts of Interest

The authors declare that they have no conflicts of interest.

Acknowledgments

References

[1] BP (British Petroleum), "BP Statistical Review of World Energy," https://www.bp.com/content/dam/bp/business-sites/en/global/corporate/pdfs/energy-economics/statistical-review/bp-stats-review-2019-full-report.pdf, 2019.

[2] IEA (International Energy Agency), "World energy outlook," https://www.iea.org/reports/world-energy-outlook-2019/gas, 2019.

[3] C. W. Spencer, "Review of characteristics of low-permeability gas reservoirs in western United States," *AAPG Bulletin*, vol. 73, no. 5, pp. 613–629, 1989.

[4] B. E. Law, "Basin-centered gas systems," *AAPG Bulletin*, vol. 86, no. 11, pp. 1891–1919, 2002.

[5] C. Zou, R. Zhu, K. Liu et al., "Tight gas sandstone reservoirs in China: characteristics and recognition criteria," *Journal of Petroleum and Science Engineering*, vol. 88-89, pp. 82–91, 2012.

[6] Y. H. Li, Y. Song, Z. X. Jiang et al., "Parameters statistic analysis of global tight sand gas basins," *Natural Gas of Geoscience*, vol. 28, no. 6, pp. 952–964, 2017.

[7] G. Shaobin, F. Juanjuan, G. Dan, L. Heyang, and H. Jiaguo, "Research status and prospects for marine-continental shale gases in China," *Petroleum Geology and Exploration*, vol. 37, no. 5, pp. 535–540, 2015.

[8] C. Jiyu, L. I. Junqian, and L. I. Chenchen, "Co-exploration potential for coalbed methane and tight sandstone gas in the middle section of the Kele syncline, Northwest Guizhou," *Coal Geology and Exploration*, vol. 46, no. 2, pp. 28–34, 2018.

[9] W. Liu, M. Chen, P. Guan et al., "Ternary geochemical tracer system for natural gas accumulation," *Science in China Series D: Earth Science*, vol. 37, no. 7, pp. 908–915, 2007.

[10] J. Dai, Y. Ni, G. Hu et al., "Composition of stable hydrocarbon isotopes in big tight -sandstone gas fields in China," *Science in China Series D: Earth Science*, vol. 44, no. 4, pp. 563–578, 2014.

[11] M. Schmitt, C. P. Fernandes, F. G. Wolf, J. A. Bellini da Cunha Neto, C. P. Rahner, and V. S. Santiago dos Santos, "Characterization of Brazilian tight gas sandstones relating permeability and angstrom-to micron-scale pore structures," *Journal of Natural Gas Science and Engineering*, vol. 27, no. 2, pp. 785–807, 2015.

[12] A. Torabi, H. Fossen, and A. Braathen, "Insight into petrophysical properties of deformed sandstone reservoirs," *AAPG Bulletin*, vol. 97, no. 4, pp. 619–637, 2013.

[13] J. Lai, G. Wang, Z. Wang et al., "A review on pore structure characterization in tight sandstones," *Earth-Science Review*, vol. 177, pp. 436–457, 2018.

[14] J. Parnell, D. Middleton, C. Honghan, and D. Hall, "The use of integrated fluid inclusion studies in constraining oil charge history and reservoir compartmentation: examples from the Jeanne d'Arc Basin, offshore Newfoundland," *Marine and Petroleum Geology*, vol. 18, no. 5, pp. 535–549, 2001.

[15] Y. Sun, X. Xi, and Z. Huang, "Studying hydrocarbon charge history in Bozhong 25-1 oilfield by fluid inclusion technique," *China Offshore Oil and Gas Geology*, vol. 16, no. 4, pp. 238–244, 2002.

[16] F. Y. Wang, X. Q. Pang, H. S. Zeng, Y. L. Shi, J. F. Hu, and K. Y. Liu, "Pale-oil leg recognition and its application to petroleum exploration," *Xinjiang Petroleum and Geology*, vol. 26, no. 5, pp. 107–111, 2005.

[17] P. Ni, H. Fan, and J. Ding, "Progress in fluid inclusions," *Bulletin of Mineralogy Petroleum and Geochemistry*, vol. 33, no. 1, pp. 1–5, 2014.

[18] I. Kaneoka and N. Takaoka, "Noble gas isotopes in Hawaiian ultramafic nodules and volcanic rocks, constraint on generic relationships," *Science*, vol. 52, no. 1, pp. 75–95, 1985.

[19] Y. Xu, P. Shen, M. Tao, and M. Sun, "Distribution of helium isotopes in natural gas of petroliferous basins in China," *Chinese Science Bulletin*, vol. 39, no. 16, pp. 1505–1508, 1994.

[20] W. Liu, X. Wang, G. Ten et al., "Research progress of gas geochemistry during the past decade in China," *Bulletin of Mineralogy Petroleum and Geochemistry*, vol. 32, no. 3, pp. 279–289, 2013.

[21] D. W. Zhang, W. H. Liu, J. J. Zheng, X. F. Wang, and Q. Y. Nan, "Identification of main gas source in Kuqa depression

using argon isotope rations," *Geochimica*, vol. 32, no. 6, pp. 38–41, 2005.

[22] R. K. McLimans, "The application of fluid inclusions to migration of oil and diagenesis in petroleum reservoirs," *Applied Geochemistry*, vol. 2, no. 5-6, pp. 585–603, 1987.

[23] M. Lisk, G. W. O'Brien, and P. J. Eadington, "Quantitative evaluation of the oil-leg potential in the Oliver gas field, Timor Sea, Australia," *AAPG Bulletin*, vol. 86, no. 9, pp. 1531–1542, 2002.

[24] C. J. Ballentine, R. Burgess, and B. Marty, "Tracing fluid origin, transport and interaction in the Crust," *Mineralogy Geochemistry*, vol. 47, no. 1, pp. 539–614, 2002.

[25] W. Liu, M. Sun, and Y. Xu, "Isotopic characteristics of natural gas and gas source correlation in Ordos Basin," *Chinese Science Bulletin*, vol. 46, no. 22, pp. 1902–1905, 2001.

[26] R. B. Warrier, M. C. Castro, C. M. Hall, and K. C. Lohmann, "Large atmospheric noble gas excesses in a shallow aquifer in the Michigan Basin as indicators of a past mantle thermal event," *Earth and Planetary Science Letters*, vol. 375, pp. 372–382, 2013.

[27] P. H. Barry, M. Lawson, W. P. Meurer et al., "Determining fluid migration and isolation times in multiphase crustal domains using noble gases," *Geology*, vol. 45, no. 9, pp. 775–778, 2017.

[28] X. Wang, G. Wang, Q. Zhao et al., "Potential for natural gas in the Liupanshui area, Western Guizhou," *Guizhou Geology*, vol. 14, no. 4, pp. 337–345, 1997.

[29] W. Luo, M. Hou, X. Liu et al., "Geological and geochemical characteristics of marine-continental transitional shale from the Upper Permian Longtan formation, Northwestern Guizhou, China," *Marine and Petroleum Geology*, vol. 89, pp. 58–67, 2018.

[30] X. Ma, S. Guo, D. Shi, Z. Zhou, and G. Liu, "Investigation of pore structure and fractal characteristics of marine- continental transitional shales from Longtan Formation using MICP, gas adsorption, and NMR (Guizhou, China)," *Marine and Petroleum Geology*, vol. 107, pp. 555–571, 2019.

[31] X. Z. Dou, B. Jiang, Y. Qin, W. Wang, and W. Y. Chen, "Structure evolution in west of Guizhou area and control to seam in late Permian," *Coal Science and Technology*, vol. 40, no. 3, pp. 109–114, 2012.

[32] X. Niu, C. Feng, and J. Liu, "Formation mechanism and time of Qianzhong uplift," *Marine Origin Petroleum Geology*, vol. 12, no. 2, pp. 46–50, 2007.

[33] C. Li, L. Li, L. Huai, Y. Wang, X. Zhang, and Z. Niu, "Coal accumulating pattern of Longtan formation coal in Guizhou Province," *Coal Technology*, vol. 34, no. 10, pp. 114–116, 2015.

[34] F. Hao, H. Zou, and Y. Lu, "Mechanisms of shale gas storage: implications for shale gas exploration in China," *AAPG Bulletin*, vol. 97, no. 8, pp. 1325–1346, 2013.

[35] S. Yulin, Q. Yong, G. Yinghai, Y. Tongsheng, S. Yubao, and J. Hongbo, "Sedimentary controlling factor of unattached multiple superimposed coalbed-methane system formation," *Earth Science*, vol. 37, no. 3, pp. 573–579, 2012.

[36] J. Zhang, X. Li, X. Zhang et al., "Geochemical and geological characterization of marine-continental transitional shales from Longtan Formation in Yangtze area, South China," *Marine and Petroleum Geology*, vol. 96, pp. 1–15, 2018.

[37] R. Wang, S. Sang, J. Jin et al., "Characteristics and significance of heterogeneity of sea-land transitional facies shale gas reservoir in North Guizhou, China," *Geosciences Journal*, vol. 23, no. 1, pp. 101–117, 2019.

[38] Y. Shen, Y. Qin, Y. Guo, T. Yi, Y. Shao, and H. Jin, "Sedimentary controlling factor of unattached multiple superimposed coalbed-methane system formation," *Earth Science*, vol. 37, no. 3, pp. 573–579, 2012.

[39] K. Ufer, H. Stanjek, G. Roth, R. Dohrmann, R. Kleeberg, and S. Kaufhold, "Quantitative phase analysis of bentonites by the Rietveld method," *Clays and Clay Minerals*, vol. 56, no. 2, pp. 272–282, 2008.

[40] N. Zhang, X. Shan, G. Ou et al., *Test Method for Fluid Inclusion in Sedimentary Basins by Microthermometry: SY/T 6010–2011*, Petroleum Industry Press, Beijing, 2011.

[41] M. Sun, "Measurement technology of noble gas isotopes in natural gases," *Acta Sedimentologica Sinica*, vol. 19, no. 2, pp. 271–275, 2001.

[42] R. L. Folk, *Petrology of Sedimentary Rocks*, Hemphill Publishing Company, Austin, TX, 1980.

[43] S. Li, S. Li, X. Shan, C. Gong, and X. Yu, "Classification, formation, and transport mechanisms of mud clasts," *International Geology Review*, vol. 59, no. 12, pp. 1609–1620, 2017.

[44] P. H. Nelson, "Pore-throat sizes in sandstones, tight sandstones, and shales," *AAPG Bulletin*, vol. 93, no. 3, pp. 329–340, 2009.

[45] C. Samakinde, M. Opuwari, and J. M. V. B. Donker, "The effects of clay diagenesis on petrophysical properties of the lower cretaceous sandstone reservoirs, Orange Basin, South Africa," *Journal of Geology*, vol. 119, no. 1, pp. 187–202, 2016.

[46] B. A. Mamyrin, G. S. Anufrriev, and I. L. Kamenskii, "Determination of the isotopic composition of atmospheric helium," *Geochemistry International*, vol. 7, pp. 498–505, 1970.

[47] J. E. Lupton, "Terrestrial inert gases: isotope tracer studies and clues to primordial components in the mantle," *Annual Review of Earth and Planetary Sciences*, vol. 11, no. 1, pp. 371–414, 1983.

[48] R. J. Poreda, P. D. Jenden, I. R. Kaplan, and H. Craig, "Mantle helium in Sacramento basin natural gas wells," *Geochimica et Cosmochimica Acta*, vol. 50, no. 12, pp. 2847–2853, 1986.

[49] C. J. Ballentine and R. K. O'Nions, "The nature of mantle neon contributions to Vienna Basin hydrocarbon reservoirs," *Earth and Planetary Science Letters*, vol. 113, no. 4, pp. 553–567, 1992.

[50] X. Wang, G. Wei, J. Li et al., "Geochemical characteristics and origins of noble gases of the Kela 2 gas field in the Tarim Basin, China," *Marine and Petroleum Geology*, vol. 89, pp. 155–163, 2018.

[51] Y. Xu, P. Shen, and W. Liu, *Geochemistry of Noble Gases in Natural Gas*, Science Press, Beijing, 1998.

[52] M. Ozima and F. A. Podosek, *Noble Gas Geochemistry*, Cambridge University Press, London, 1983.

[53] X. Wang, J. Wang, and Y. Hu, "On metallogenic depth and metallogenic epoch determined by burial history— with case study of Qinglong antimony deposit," *Jiangxi Science*, vol. 29, no. 2, pp. 200–206, 2011.

[54] Z. Wu, X. Liu, X. Li, X. Wang, and J. Zheng, "The application of noble gas isotope in gas-source correlation of Yuanba reservoir, Sichuan Basin," *Natural Gas Geoscience*, vol. 28, no. 7, pp. 1072–1077, 2017.

[55] W. Liu and Y. Xu, *Relationship between Argon in natural gas and Potassium-Argon in source rock and reservoirs//annual report in 1986 of the Open Research Laboratory of Biology and Gas Geochemistry of Lanzhou Institute of Geology, Chinese*

Academy of Sciences, Gansu Science and Technology Press, Gansu, 1987.

[56] D. Ren, D. Xu, J. Zhang, and F. Zhang, "Distribution of associated elements in coals from Shenbei Coalfield," *Journal of China University of Mining &Technology*, vol. 28, no. 1, pp. 5–8, 1999.

[57] X. Pang, M. Li, S. Li, and Z. Jin, "Geochemistry of petroleum systems in the Niuzhuang South Slope of Bohai Bay Basin: Part 3. Estimating hydrocarbon expulsion from the Shahejie formation," *Organic Geochemistry*, vol. 36, no. 4, pp. 497–510, 2005.

[58] J. Peng, X. Pang, H. Shi et al., "Hydrocarbon generation and expulsion characteristics of Eocene source rocks in the Huilu area, northern Pearl River Mouth basin, South China Sea: implications for tight oil potential," *Marine and Petroleum Geology*, vol. 72, pp. 463–487, 2016.

[59] F. Wang and S. Guo, "Shale gas content evolution in the Ordos Basin," *International Journal of Coal Geology*, vol. 211, no. 103231, 2019.

[60] Z. Liu, S. Guo, and R. Lv, "Shale-gas play risk of the lower Cambrian on the Yangtze platform, South China," *AAPG Bulletin*, vol. 104, no. 5, pp. 989–1009, 2020.

[61] R. M. Bustin and C. R. Clarkson, "Geological controls on coalbed methane reservoir capacity and gas content," *International Journal of Coal Geology*, vol. 38, no. 1–2, pp. 3–26, 1998.

[62] D. Xia, Z. Wang, and J. Ma, "Analyses on the adsorption difference between coalbed methane and shale gas," *Coal Geology and Exploration*, vol. 43, no. 6, pp. 36–38, 2015.

[63] Z. Cao, H. Jiang, J. Zeng et al., "Nanoscale liquid hydrocarbon adsorption on clay minerals: a molecular dynamics simulation of shale oils," *Chemical Engineering Journal*, vol. 420, article 127578, 2021.

[64] J. M. Hunt, *Petroleum Geochemistry and Geology*, Freeman and Co., New York, W. H, 2d ed. edition, 1996.